

# Imaging orbital-selective quasiparticles in the Hund's metal state of FeSe

A. Kostin<sup>1,2,10</sup>, P. O. Sprau<sup>1,2,10</sup>, A. Kreisel<sup>3,10</sup>, Yi Xue Chong<sup>1,2</sup>, A. E. Böhmer<sup>4,5</sup>, P. C. Canfield<sup>4,6</sup>, P. J. Hirschfeld<sup>7</sup>, B. M. Andersen<sup>10</sup> and J. C. Séamus Davis<sup>1,2,9\*</sup>

**Strong electronic correlations, emerging from the parent Mott insulator phase, are key to copper-based high-temperature superconductivity. By contrast, the parent phase of an iron-based high-temperature superconductor is never a correlated insulator. However, this distinction may be deceptive because Fe has five activated *d* orbitals while Cu has only one. In theory, such orbital multiplicity can generate a Hund's metal state, in which alignment of the Fe spins suppresses inter-orbital fluctuations, producing orbitally selective strong correlations. The spectral weights  $Z_m$  of quasiparticles associated with different Fe orbitals  $m$  should then be radically different. Here we use quasiparticle scattering interference resolved by orbital content to explore these predictions in FeSe. Signatures of strong, orbitally selective differences of quasiparticle  $Z_m$  appear on all detectable bands over a wide energy range. Further, the quasiparticle interference amplitudes reveal that  $Z_{xy} < Z_{xz} \ll Z_{yz}$ , consistent with earlier orbital-selective Cooper pairing studies. Thus, orbital-selective strong correlations dominate the parent state of iron-based high-temperature superconductivity in FeSe.**

The undoped phase proximate to superconductivity in copper-based materials is a strong Mott insulator<sup>1,2</sup>, while that proximate to iron-based superconductivity is generally of a metallic nature<sup>3,4</sup>. This has motivated a perception that the mechanisms of high-temperature superconductivity (HTS) must be quite different in these two canonical materials classes and, moreover, that strong electronic correlations are not indispensable to HTS. Importantly, however, the electronic structure of the iron-based materials can still be governed by intense electronic correlations if an orbital-selective Hund's metal state exists<sup>5–13</sup>. This remarkable situation was discovered in theoretical studies of the multi-orbital Hubbard model (Supplementary Information, Introduction), which typically consider the intra-orbital Hubbard energy  $U$ , the inter-orbital Coulomb interaction energy  $U'$  ( $=U-2J$  for spin-rotational symmetry), and the inter-orbital Hund interaction energy  $J$  between spins. For a range of strong  $J$ , dynamical mean-field theory<sup>2</sup> predicts that inter-orbital charge fluctuations are greatly suppressed, leading to an orbital decoupling of the strong correlations<sup>6–13</sup>. The striking consequence is that strongly correlated and thus low-coherence states associated with one orbital are predicted to coexist with coherent delocalized quasiparticle states associated with the other.

In theory, Hund's metals occur in a region of intermediate to strong  $U$  and of strong  $J$  (refs 5–13). They are dominated by orbital-selective correlations, with the result that quasiparticle weights  $Z_m$  associated with different orbitals  $m$  diminish differently with increasing  $J$  or  $U$ . The quasiparticle weight  $Z$  is given by  $Z(\mathbf{k}) = (1 - \partial \text{Re} \Sigma(\mathbf{k}, \omega) / \partial \omega |_{\omega=0})^{-1}$ , where  $\Sigma(\mathbf{k}, \omega) = \text{Re} \Sigma(\mathbf{k}, \omega) + i \text{Im} \Sigma(\mathbf{k}, \omega)$  is the self-energy of a quasiparticle state  $|\mathbf{k}\rangle$  with momentum  $\hbar\mathbf{k}$  that is subject to strong electron–electron interactions. The quasiparticle weight on band  $j$  in  $\mathbf{k}$ -space,  $Z_j(\mathbf{k})$ , can be connected to the quasiparticle weight in orbital space  $Z_m$  via the matrix

elements of a unitary transformation. Multi-band Hubbard theories also exhibit orbital-selective quasiparticle (OSQP) phenomenology in which  $Z_m$  evolves differently for each orbital  $m$  (refs 2,7,9,10,14–16). Moreover, when orbital degeneracies are lifted, for example by crystal field splitting in an orthorhombic/nematic phase, this further suppresses inter-orbital charge fluctuations and amplifies the orbital decoupling that generates the OSQP<sup>7,9–11,14–17</sup>. One approach to identifying such orbital-selective strong correlations experimentally would be to demonstrate that  $Z(\mathbf{k})$  is highly distinct between the regions of the electronic bands that are associated with each different orbital  $m$ .

Because Fe-based materials supporting Fe-based superconductivity are excellent candidates to exhibit Hund's metal orbital-selective effects, focus has naturally turned to detecting and understanding such phenomena in these systems. The resulting plethora of theoretical predictions<sup>6,8,11,13,15</sup> include the following: (1) the electronic structure of Fe-based superconductors should be heavily influenced by orbital-selective strong correlations, (2) this effect is caused primarily by the Hund's decoupling of the inter-orbital charge fluctuations, (3) the strength of correlations in each decoupled band  $k_j(E)$  grows as it approaches half filling and (4) when orbital-selective strong correlations exist in such a state, Cooper pairing itself may become orbital selective<sup>6,18–21</sup>. Recent photoemission studies of orbital-dependent bandwidth renormalization in these materials<sup>22</sup> has been interpreted in this way. However, a capability to directly visualize the orbital selectivity of the quasiparticles in the normal state of Fe-based HTS materials, ideally simultaneously with visualization of the electronic structures of the superconducting and nematic phases<sup>3,4</sup>, remains an urgent priority.

To address this challenge, we focus on the compound FeSe, which shows clear indications of orbital selectivity<sup>6,15</sup>. The FeSe crystal unit cell has  $a=5.31 \text{ \AA}$ ,  $b=5.33 \text{ \AA}$  and  $c=5.49 \text{ \AA}$  in the

<sup>1</sup>Department of Physics, Cornell University, Ithaca, NY, USA. <sup>2</sup>CMPMS Department, Brookhaven National Laboratory, Upton, NY, USA. <sup>3</sup>Institut für Theoretische Physik, Universität Leipzig, Leipzig, Germany. <sup>4</sup>Ames Laboratory, U.S. Department of Energy, Ames, IA, USA. <sup>5</sup>Karlsruhe Institute of Technology, Karlsruhe, Germany. <sup>6</sup>Department of Physics and Astronomy, Iowa State University, Ames, IA, USA. <sup>7</sup>Department of Physics, University of Florida, Gainesville, FL, USA. <sup>8</sup>Niels Bohr Institute, University of Copenhagen, Copenhagen, Denmark. <sup>9</sup>School of Physics and Astronomy, University of St. Andrews, Fife, UK. <sup>10</sup>These authors contributed equally: A. Kostin, P.O. Sprau, A. Kreisel. \*e-mail: [jseamusdavis@gmail.com](mailto:jseamusdavis@gmail.com)

orthorhombic/nematic phase below structural transition temperature  $T_s \cong 90$  K. Specifics of the Fe plane of the same lattice can be described using the two inequivalent Fe–Fe distances  $a_{\text{Fe}} = 2.665$  Å and  $b_{\text{Fe}} = 2.655$  Å. The Fermi surface consists of three bands for which an accurate tight-binding model  $H_{\mathbf{k}}^{tb}$  has been developed<sup>18</sup>. This model has excellent simultaneous consistency with angle-resolved photoemission<sup>23–25</sup>, quantum oscillations<sup>26–28</sup> and Bogoliubov quasiparticle interference (QPI)<sup>18,19</sup>. Surrounding the  $\Gamma = (0,0)$  point is an ellipsoidal hole-like  $\alpha$ -band, whose Fermi surface  $\mathbf{k}_{\alpha}(E=0)$  has its major axis aligned to the orthorhombic  $b$ -axis; surrounding the  $X = (\pi/a_{\text{Fe}}, 0)$  point is the electron-like  $\varepsilon$ -band, whose ‘bowtie’ Fermi surface  $\mathbf{k}_{\varepsilon}(E=0)$  has its major axis aligned to the orthorhombic  $a$ -axis; surrounding the  $Y = (0, \pi/b_{\text{Fe}})$  point, a  $\delta$ -band Fermi surface should also exist but has proven difficult to detect by spectroscopic techniques. Moreover, it was recently realized that orbital-selective Cooper pairing<sup>18,21</sup> of predominantly the  $d_{yz}$  electrons causes the highly unusual superconducting energy gaps  $\Delta_{\alpha}(\vec{k})$  and  $\Delta_{\varepsilon}(\vec{k})$  of FeSe (refs<sup>18,19</sup>), from whose structure the FeSe quasiparticle weights are estimated to be  $Z_{xy} \sim 0.1$ ,  $Z_{xz} \sim 0.2$  and  $Z_{yz} \sim 0.8$  (with the other  $Z$  values being irrelevant for energies near  $E=0$ ; ref.<sup>18</sup>). The challenge is to discover if all these exotic phenomena are indeed caused by the existence of orbital-selective strong correlations in a Hund’s metal normal state of FeSe.

Imaging of QPI<sup>29</sup> is an attractive approach. QPI has become widely used to determine exotic electronic structure of correlated electronic materials<sup>30–35</sup>. This effect occurs when an impurity atom/vacancy scatters quasiparticles, which then interfere quantum-mechanically to produce characteristic modulations of the density of states  $\delta N(\mathbf{r}, E)$  surrounding each impurity site; the global effects of this random impurity scattering are usually studied by using  $\delta N(\mathbf{q}, E)$ , the Fourier transform of  $\delta N(\mathbf{r}, E)$ . In a multi-orbital context, this can be predicted using

$$\delta N(\mathbf{q}, E) = -1 / \pi \text{Tr} \left( \text{Im} \sum_{\mathbf{k}} \hat{G}_{\mathbf{k}}(E) \hat{T}(E) \hat{G}_{\mathbf{k}+\mathbf{q}}(E) \right), \quad (1)$$

where  $G_{nmk} = \sqrt{Z_n Z_m} G_{nmk}^0$  with  $\hat{G}_{\mathbf{k}}^0(E) = ((E + i\eta)\hat{I} - \hat{H}_{\mathbf{k}}^{tb})^{-1}$  is the electron’s Green’s function in orbital space and  $\hat{T}(E)$  is a matrix representing all the possible scattering processes between states  $|\mathbf{k}\rangle$  and  $|\mathbf{k}+\mathbf{q}\rangle$  for an impurity with on-site potential. Atomic-scale imaging of these interference patterns  $\delta N(\mathbf{r}, E)$  is achieved using spatial mapping of differential tunnelling conductance  $dI/dV(\mathbf{r}, E) \equiv g(\mathbf{r}, E)$ , and has developed into a high-precision technique for measurement of the electronic band structure  $\mathbf{k}_{\mathbf{s}}(E)$  of strongly correlated electron fluids<sup>31–34</sup>. QPI should be of unique utility in searching for both orbital-selective coherence and spectral weight because (1) the existence of quantum interference is itself a robust test of  $\mathbf{k}$ -space coherence and (2) the amplitude of QPI signals is sensitive as the squares of quasiparticle weights (equation 1). Our target is thus to achieve orbitally resolved QPI from which the relative  $Z_m$  values of the normal state quasiparticles can be estimated.

We pursue this objective in the iron-based superconducting compound FeSe. Figure 1a is a schematic representation of the orbitally resolved band structure of FeSe at  $k_z=0$  (ref.<sup>18</sup>). Surrounding the  $\Gamma = (0,0)$  point, the evolution of  $\mathbf{k}_{\alpha}(E)$  is hole-like with the band top near  $E=+15$  meV and  $d_{yz}$  orbital character (green) maximum along the  $x$ -axis while  $d_{xz}$  orbital character (red) prevails along the  $y$ -axis. Centred on the  $X = (\pi/a_{\text{Fe}}, 0)$  point,  $\mathbf{k}_{\varepsilon}(E)$  exhibits electron-like evolution with two Dirac points near  $E=-25$  meV, and  $d_{yz}$  orbital character (green) dominant along the  $y$ -axis while  $d_{xy}$  orbital character (blue) prevails along the  $x$ -axis. A fully coherent  $\delta$ -band at the  $Y = (0, \pi/b_{\text{Fe}})$  point would then have  $d_{xz}$  orbital character (red) dominant along the  $x$ -axis and  $d_{xy}$  orbital character (blue) prevailing along the  $y$ -axis. Figure 1c,g shows the orbitally resolved constant-energy contours (CECs)  $\mathbf{k}_{\alpha}(E=-10$  meV)

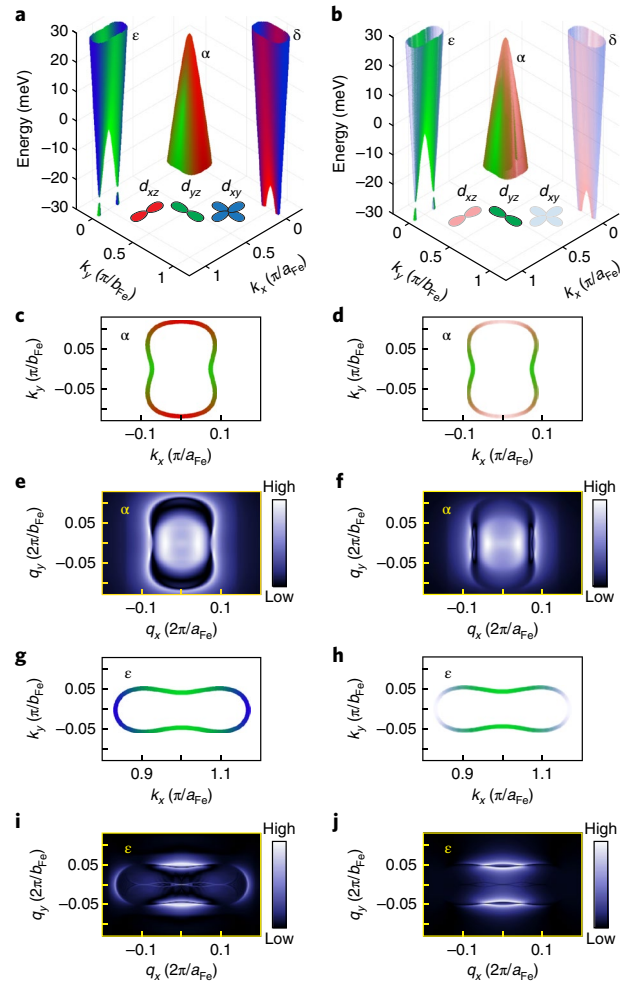


**Fig. 1 | Orbitally resolved quasiparticle scattering interference (QPI) in FeSe.**

**a**, Schematic representation of orbitally resolved band structure of FeSe at  $k_z=0$ . For each fully coherent quasiparticle state  $|\mathbf{k}\rangle$  in these bands, green represents  $d_{yz}$  orbital content, red represents  $d_{xz}$  orbital content and blue represents  $d_{xy}$  orbital content. The two Dirac points on the band surrounding the  $X$ -point  $(\pi/a_{\text{Fe}}, 0)$  occur near  $E=-25$  meV while the top of the hole-like band surrounding the  $\Gamma$ -point  $(0,0)$  is close to  $E=+15$  meV. **b**, Schematic representation of the same orbitally resolved band structure of FeSe at  $k_z=0$  but now indicating the effects of different quasiparticle weight  $Z$ . Here green represents the virtually fully coherent  $d_{yz}$  orbital content, translucent red represents the reduced  $Z$  value of  $d_{xz}$  orbital content and pale blue represents  $d_{xy}$  orbital content where  $Z$  tends towards zero. **c**, Orbital content of CECs at the  $\Gamma$ -point  $(0,0)$  at  $-10$  meV using the same colour code as **a**. **d**, Orbital content of CECs at the  $\Gamma$ -point  $(0,0)$  at  $-10$  meV using the same colour code as **b**. **e**, Anticipated  $|\delta N_{\alpha}(\mathbf{q}, E=-10 \text{ meV})|$  QPI signature of intraband scattering interference within the  $\alpha$ -band surrounding the  $\Gamma$ -point, for quasiparticle weights  $Z_{xy}=Z_{xz}=Z_{yz}=1$ . The  $|\delta N(\mathbf{q}, E)| \equiv \left| \frac{1}{\pi} \text{Tr} \text{Im} \sum_{\mathbf{k}} \hat{G}_{\mathbf{k}}(E) \hat{T}(E) \hat{G}_{\mathbf{k}+\mathbf{q}}(E) \right|$  images in **e,f,i,j** are calculated using the  $T$ -matrix with weak impurity potential and the band-structure model displayed in **a,b**. In the calculations, the  $\mathbf{k}$  sum was restricted to the appropriate region of the Brillouin zone to separately capture the intraband scattering interference pattern for different pockets. **f**, Anticipated  $|\delta N_{\alpha}(\mathbf{q}, E=-10 \text{ meV})|$  QPI signature for the  $\alpha$ -band with OSQP weights  $Z_{xy} \approx 0.1$ ,  $Z_{xz} \approx 0.2$  and  $Z_{yz} \approx 0.8$ . **g**, Orbital content of CEC at the  $X$ -point  $(\pi/a_{\text{Fe}}, 0)$  at  $+10$  meV using the same colour code as **a**. **h**, Orbital content of CECs at the  $X$ -point  $(\pi/a_{\text{Fe}}, 0)$  at  $+10$  meV using the same colour code as **b**. **i**, Anticipated  $|\delta N_{\varepsilon}(\mathbf{q}, E=+10 \text{ meV})|$  QPI signature of intraband scattering interference within the  $\varepsilon$ -band for quasiparticle weights  $Z_{xy}=Z_{xz}=Z_{yz}=1$ . **j**, Anticipated  $|\delta N_{\varepsilon}(\mathbf{q}, E=+10 \text{ meV})|$  QPI signature for the  $\varepsilon$ -band with OSQP weights  $Z_{xy} \approx 0.1$ ,  $Z_{xz} \approx 0.2$  and  $Z_{yz} \approx 0.8$ .

and  $\mathbf{k}_\epsilon(E=+10\text{ meV})$  of the  $\alpha$ - and  $\epsilon$ -bands in Fig. 1a. Figure 1e,i then shows the expectations based on equation (1) for the intraband QPI intensity patterns  $|\delta N_\alpha(\mathbf{q}, E=-10\text{ meV})|$  and  $|\delta N_\epsilon(\mathbf{q}, E=+10\text{ meV})|$  corresponding to these contours, if all  $|\mathbf{k}\rangle$  states are equally and fully coherent. If, by contrast, OSQPs exist in FeSe, QPI should be very different because the quasiparticle weights  $Z_m$  associated with the Fe  $d$  orbitals could all be distinct. In that situation, one might expect to see phenomena exemplified schematically by Fig. 1b. Here, for didactic purposes, we have chosen  $Z_{xy} < Z_{xz} \ll Z_{yz}$ . This means that in  $\mathbf{k}_\alpha(E)$  the quasiparticle weight of  $d_{yz}$  orbital character (green) along the  $x$ -axis dominates strongly over the quasiparticle weight of  $d_{xz}$  orbital character (translucent red) along the  $y$ -axis (Fig. 1d). Similarly, for  $\mathbf{k}_\epsilon(E)$  the quasiparticle weight of  $d_{yz}$  orbital character dominates strongly along the  $y$ -axis when compared with the negligible quasiparticle weight of the  $d_{xy}$  orbital character (pale blue) along the  $x$ -axis (Fig. 1h). The  $\delta$ -band exhibits feeble quasiparticle weight of  $d_{xz}$  orbital character along the  $x$ -axis and negligible  $d_{xy}$  quasiparticle weight along the  $x$ -axis. Under these circumstances, the QPI patterns will obviously be very different because scattering between regions with  $Z_m \ll 1$  will produce far weaker intensity modulations. Thus, Fig. 1f,j shows the anticipated intraband QPI intensity patterns  $|\delta N_\alpha(\mathbf{q}, E=-10\text{ meV})|$  and  $|\delta N_\epsilon(\mathbf{q}, E=+10\text{ meV})|$ , when the  $|\mathbf{k}\rangle$  states have quasiparticle weights  $Z_{xy} < Z_{xz} \ll Z_{yz}$ . These are obviously quite different from those expected of fully coherent CECs in Fig. 1e,i, for the obvious reason that weak QPI intensity is produced by the quasiparticles of  $d_{xz}$  orbital character and virtually none by those of  $d_{xy}$  orbital character (Supplementary Information Section II).

For FeSe, quantitative comparison of the QPI signature  $\delta N(\mathbf{q}, E)$  expected for fully coherent bands versus strong orbital selectivity of quasiparticles can then be carried out by using the  $T$ -matrix formalism. Here, the fully coherent Green's function  $\hat{G}_\mathbf{k}^0(E)$  representing each  $|\mathbf{k}\rangle$  state (a  $5 \times 5$  matrix retaining orbital content information) is computed directly from the parameters of the electron band structure (Fig. 1a). These  $\hat{G}_\mathbf{k}^0(E)$  are then used to calculate  $\delta N(\mathbf{q}, E)$  from equation 1. A scattering matrix  $\hat{T}(E) = V_{\text{imp}} \hat{I} (1 - V_{\text{imp}} \sum_{\mathbf{k}} \hat{G}_\mathbf{k}^0(E))^{-1}$  representing  $Z_m = 1$  for all  $m$  and a  $\delta$ -function scattering potential at the origin in real space, and only  $|\mathbf{k}\rangle$  for which  $k_z = 0$ , are used (Supplementary Information Section II). Additionally, we numerically calculate the Fourier transform amplitude of the Feenstra transform,  $L(\mathbf{r}, E) = N(\mathbf{r}, E) / \int N(\mathbf{r}, E') dE'$ , to compare directly with the measured normalized conductance,  $(dI/dV)/(IV)$  (see below and Supplementary Information Section II). The resulting  $|L(\mathbf{q}, E)|$  for fully coherent FeSe  $|\mathbf{k}\rangle$  states are shown in Fig. 2a–d (and in Supplementary Video 1). These  $|L(\mathbf{q}, E)|$  comprise QPI of  $\alpha$ -,  $\epsilon$ - and  $\delta$ -bands for low- $\mathbf{q}$  scattering events. They show all the salient QPI features of fully coherent bands. By contrast, the QPI signatures of an OSQP in FeSe are determined using equation 1 but with  $G_{nm\mathbf{k}}(E) = \sqrt{Z_n} \sqrt{Z_m} G_{nm\mathbf{k}}^0(E)$ , where  $Z_m \in (0.073, 0.94, 0.16, 0.85, 0.36)$  for  $m \in (d_{xy}, d_{x^2-y^2}, d_{xz}, d_{yz}, d_{z^2})$  and  $V_{\text{imp}}$  is the same as before (Supplementary Information Section II). (Although these specific values chosen were taken from ref. 18, the data in this paper as well as the data in ref. 18 are consistent with the orbitally selective ansatz within a range of  $Z$  values that are all consistent with the inequality  $Z_{xy} < Z_{xz} \ll Z_{yz}$ .) Most relevant are the orbitally resolved quasiparticle weights  $Z_{xy} \approx 0.1$ ,  $Z_{xz} \approx 0.2$  and  $Z_{yz} \approx 0.8$ , with the other two orbitals having negligible spectral weight near  $E=0$ . The predicted  $|L(\mathbf{q}, E)|$  for the OSQP are shown in Fig. 2i–l (and in Supplementary Video 2). These  $L(\mathbf{q}, E)$  are now dominated by QPI of both  $\alpha$ - and  $\epsilon$ -bands, as scattering in the  $\delta$ -band is strongly suppressed due to decoherence of the respective quasiparticles. For the OSQP scenario, the scattering intensity distribution is strikingly  $C_2$  symmetric. As expected, the QPI is dominated by quasiparticles with  $d_{yz}$  orbital content, which are oriented along the  $k_x$ -axis in the

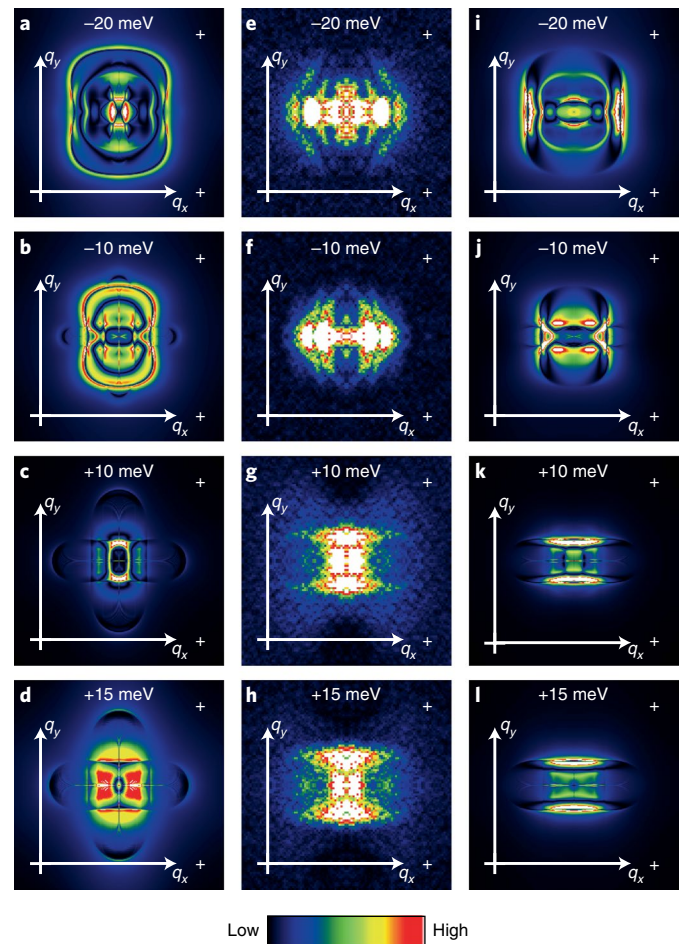


**Fig. 2 | Visualizing orbital-selective quasiparticle interference (QPI).**

**a–d**, Predicted energy-resolved  $|L(\mathbf{q}, E)|$  QPI signature of intraband scattering interference in a fully coherent state for quasiparticle weights  $Z_{xy} = Z_{yz} = Z_{xz} = 1$ . The white crosses correspond to  $\frac{3}{16} \left( \frac{2\pi}{a_{\text{Fe}}}, \frac{2\pi}{b_{\text{Fe}}} \right)$  points in the momentum space.  $|L(\mathbf{q}, E)|$  is the amplitude of the Fourier transform of the normalized conductance ( $\equiv \frac{dI}{dV} / \left( \frac{I}{V} \right)$ ) at wavevector  $\mathbf{q}$  and energy  $E$ . **e–h**, Measured  $|L(\mathbf{q}, E)|$  of FeSe at the same energies as shown in **a–d** and **i–l**. For all these energies, the measurements agree much better with the orbital selective quasiparticle (OSQP) scenario (**i–l**) than with the fully coherent QPI (**a–d**). **i–l**, Predicted energy-resolved  $|L(\mathbf{q}, E)|$  QPI signature of intraband scattering interference in an OSQP with quasiparticle weights  $Z_{xy} \approx 0.1$ ,  $Z_{xz} \approx 0.2$  and  $Z_{yz} \approx 0.8$ .

$\alpha$ -band for  $E < 0$  and concentrated along the  $k_y$ -axis in the  $\epsilon$ -band for  $E > 0$ . This produces the marked rotation of the QPI pattern by  $90^\circ$  just above the chemical potential, a remarkable effect characteristic of FeSe (ref. 34) whose origin has until now proven elusive. Clearly the QPI predictions for OSQP (Fig. 2i–l and Supplementary Video 2) are vividly different from those expected of a fully coherent conventional band structure (Fig. 2a–d and Supplementary Video 1).

Our experimental search for OSQP phenomena uses spectroscopic imaging scanning tunnelling microscopy (SI-STM) to study FeSe. The samples are inserted into the SI-STM instrument and cleaved in cryogenic ultrahigh vacuum at  $T < 20\text{ K}$ . To focus on the normal state of FeSe, measurements for the energy range from  $-8.75\text{ meV}$  to  $+8.75\text{ meV}$  are acquired at  $10.0\text{ K} > T_C$ , and the rest of the measurements are acquired at  $4.2\text{ K}$  to reduce thermal smearing. We have checked that the observed QPI phenomena do not differ between  $4.2\text{ K}$  and  $10.0\text{ K}$  (see Supplementary Information Section VIII). Differential tunnelling conductance  $g(\mathbf{r}, E) \equiv dI/dV(\mathbf{r}, E = eV)$  measurements are carried out with atomic resolution and register,

as a function of both location  $\mathbf{r}$  and electron energy  $E$ . Because of the tiny areas of FeSe bands in  $\mathbf{k}$ -space (Fig. 1a), intraband QPI wavevectors are limited,  $|\mathbf{q}(E)| < 0.25 \left(\frac{2\pi}{a_{\text{Fe}}}\right)$ , so that high-precision  $g(\mathbf{r}, E)$  imaging in very large fields of view (typically  $50 \times 50 \text{ nm}^2$ ) is required. The Fourier transform of  $g(\mathbf{r}, E)$ ,  $g(\mathbf{q}, E)$ , can then be used to reveal wavevectors and intensities of dispersive modulations due to QPI. However, to avoid artifacts (Supplementary Information Section III) images of  $L(\mathbf{r}, E = eV) \equiv \left(\frac{g(\mathbf{r}, E)}{I(\mathbf{r}, E)}\right) V$  are more typically used, and these faithfully portray relative intensity in different directions in  $\mathbf{q}$ -space<sup>34</sup>. Thus, Fig. 2e–h shows the measured  $|L(\mathbf{q}, E)|$ , the Fourier transform amplitude of  $L(\mathbf{r}, E)$ , from FeSe samples where the only scattering defects in the field of view (FOV) are at Fe sites (a topograph of the measurement FOV is shown in Supplementary Information Section IV and  $|L(\mathbf{q}, E)|$  is provided as Supplementary Video 3). All such QPI data rotate by  $90^\circ$  when measurements of  $|L(\mathbf{q}, E)|$  are made in the orthogonal orthorhombic domain (Supplementary Information Section V). Comparison of the measured QPI in Fig. 2e–h with predicted  $|L(\mathbf{q}, E)|$  for fully coherent bands (Fig. 2a–d) and for OSQP (Fig. 2i–l) reveals that the latter are in far better agreement. The intensity pattern and energy dispersion of the  $\mathbf{q}$ -vectors of maximum scattering intensity in measured  $|L(\mathbf{q}, E)|$  closely follow those shown in Fig. 2i–l, including the strong unidirectionality and the sudden rotation of dispersion direction as  $E=0$  is crossed. This provides a direct signature of OSQP in the metallic state of FeSe.

To visualize the impact of orbital selectivity on the complete band structure more globally, one can compare the energy dispersions continuously by comparing computed  $|L(q_x, E)|$  and  $|L(q_y, E)|$  with measured  $|L(q_x, E)|$  and  $|L(q_y, E)|$  respectively. For this purpose, Fig. 3a shows the theoretical dispersion of QPI maxima for  $\alpha$ -,  $\varepsilon$ -, and  $\delta$ -bands along both  $q_x$  and  $q_y$ , resolved by orbital content using the same colour code as elsewhere. Figure 3b shows the energy dependence of the predicted intensity of intraband scattering interference, along the same two trajectories as in Fig. 3a for fully coherent quasiparticle weights in all three orbitals,  $Z_{xy}=Z_{yz}=Z_{xz}=1$ . Figure 3c shows the measured intensity of intraband scattering interference along  $q_x$  and  $q_y$ . The correspondence of these data to predictions in Fig. 3b is rather poor. However, in Fig. 3d we show the predicted intensity of intraband scattering interference if FeSe exhibits orbital-selective QPI. The same two  $E$ - $q$  planes as in Fig. 3b,c are shown, but now the OSQP quasiparticle weights are  $Z_{xy} \approx 0.1$ ,  $Z_{xz} \approx 0.2$  and  $Z_{yz} \approx 0.8$ . The correspondence between experimental  $|L(\mathbf{q}, E)|$  (Fig. 3c) and the QPI signature of OSQP (Fig. 3d) is good and is discernibly superior to that in Fig. 3b.

If the quasiparticle weights do indeed obey the relation  $Z_{xy} < Z_{xz} \ll Z_{yz}$ , this begs the question of whether weak QPI can be observed on the  $\delta$ -band in its sections dominated by  $d_{xz}$  orbital content. Such phenomena should be clearest at states  $E > 10 \text{ meV}$  (because the QPI from the  $\alpha$ -band has disappeared here) and should appear along  $q_x$  due to scattering interference between  $d_{xz}$ -dominated quasiparticles connected by a double-headed arrow shown in Fig. 4a. As seen in Fig. 4b, the expected scattering of states on the  $\delta$ -pocket is significantly suppressed. The remaining panels of Fig. 4 demonstrate that there is indeed a dispersive signal along  $q_x$  at somewhat higher  $q$  than the significantly stronger scattering interference along  $q_y$  from the  $d_{yz}$  sections of the  $\varepsilon$ -band. Detailed analysis and comparison of these two electron-like dispersive signals with simulation allow the conclusion that even the  $d_{xz}$  orbital content quasiparticles with very low  $Z_{xz}$  are detectable, as expected, in the  $\delta$ -band (Supplementary Information Section VI).

Finally, to visualize approximately how the  $Z_j(\mathbf{k})$  evolve with  $\mathbf{k}$ -space angle around the Fermi surfaces of the  $\alpha$ - and  $\varepsilon$ -bands, we measure the magnitude of  $L(\mathbf{q}, E)$  on the  $\mathbf{q}$ -space trajectory through the QPI data for both bands. Figure 5a,b shows the measured angular dependence of QPI intensity for intraband scattering within the

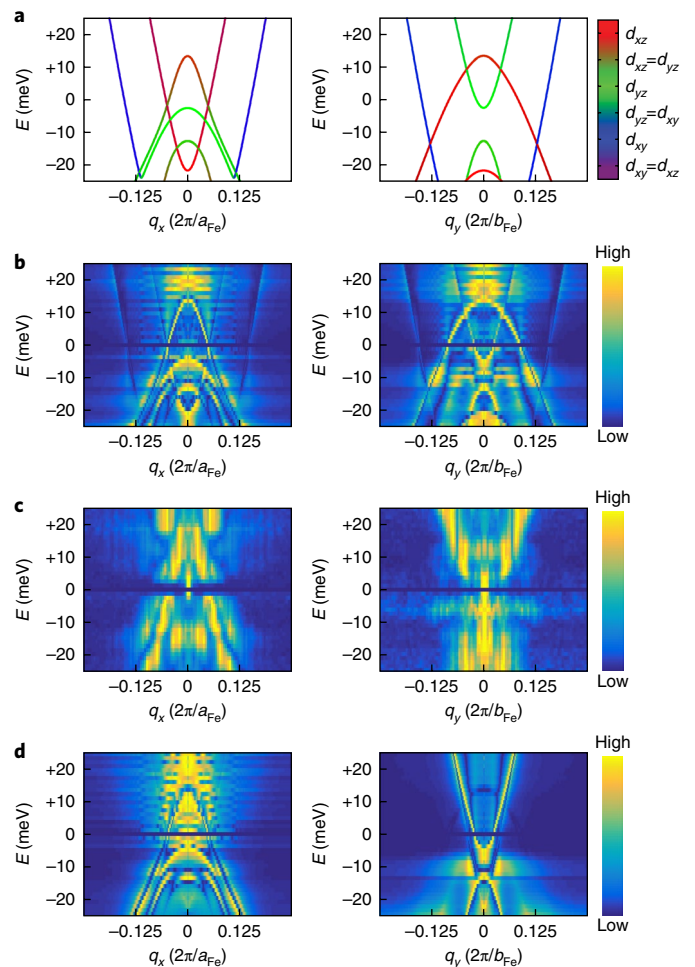


**Fig. 3 | Energy dependence of orbital-selective quasiparticle interference (QPI).** **a**, Momentum-space representation of intraband QPI maxima resolved by orbital content. Two  $E$ - $q$  (energy-wavevector) planes are shown, parallel to  $q_x$  and to  $q_y$ . The colour code shows the orbital content. **b**, Predicted intensity of intraband scattering interference for a fully coherent state. Two  $E$ - $q$  planes are shown, parallel to  $q_x$  and to  $q_y$ . The quasiparticle weights are  $Z_{xy}=Z_{yz}=Z_{xz}=1$ . **c**, Measured intensity of intraband scattering interference in FeSe. The same two  $E$ - $q$  planes as in **b** are shown. Correspondence of these data to predictions in **b** is poor, whereas their correspondence to the orbital-selective QPI prediction in **d** is much better. **d**, Predicted intensity of intraband scattering interference for OSQPs in FeSe. The same two  $E$ - $q$  planes as in **b** are shown. The OSQP quasiparticle weights here are  $Z_{xy} \approx 0.1$ ,  $Z_{xz} \approx 0.2$  and  $Z_{yz} \approx 0.8$ . Images in **b-d** are generated from  $q_x$  and  $q_y$  line cuts of the corresponding calculated and measured  $|L(\mathbf{q}, E)|$ . These cuts are normalized to unity for each energy to enhance the visibility of the band dispersions.

$\alpha$ - and  $\varepsilon$ -bands. The assignment of the scattering intensity to the electron and hole bands can be made by observing the dispersion of the intensity as a function of energy. In both cases, we focus on the trajectory of  $\mathbf{q}=2\mathbf{k}$  intraband scattering as indicated by the white crosses, at which a local maximum in QPI amplitude is detected; the data are shown in full detail versus energy in Supplementary Information Section VII. The  $L(\mathbf{q}, E)$  amplitude is determined by taking line cuts through the measured  $|L(\mathbf{q}, E)|$  maps (Fig. 5a,b) for a sequence of angles at a specified energy. Each line cut was fitted to a sum of a linear background and a Gaussian peak to determine the QPI signal amplitude (Supplementary Information Section VII). The analysis was carried out for a sequence of energies ( $-25 \text{ meV}$  to

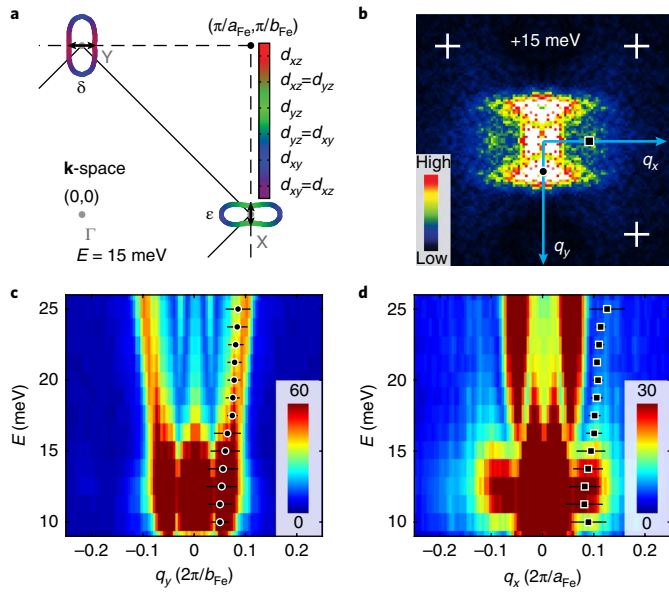


**Fig. 4 | Detecting orbital-selective QPI from both  $\epsilon$ - and  $\delta$ -bands above Fermi energy  $E_F$ .** **a**, Quasiparticle constant-energy contours at  $E = +15$  meV showing the  $\epsilon$ - and  $\delta$ -bands. The colour code indicates whether the quasiparticles are dominated by  $d_{yz}$ ,  $d_{xz}$  or  $d_{xy}$  orbital character. Double-headed arrows show scattering vectors along  $q_x$  and  $q_y$ . **b**, Measured  $|L(\mathbf{q}, E = +15 \text{ meV})|$  image. The directions of  $q_x$  and  $q_y$  line cuts are shown as blue lines. The signals from  $\epsilon$ - and  $\delta$ -bands are marked by a black circle and a black square, respectively. Signal locations were determined from fits to the line cuts (Supplementary Information Section VI). The white crosses correspond to  $\frac{3}{16} \left( \frac{2\pi}{a_{\text{Fe}}}, \frac{2\pi}{b_{\text{Fe}}} \right)$  points in  $q$ -space.  $|L(\mathbf{q}, E)|$  is the amplitude of the Fourier transform of the normalized conductance ( $\equiv \left( \frac{dI}{dV} \right) / \left( \frac{I}{V} \right)$ ) at wavevector  $\mathbf{q}$  and energy  $E$ . **c**,  $E$ - $q_y$  line cut through the sequence of measured  $|L(\mathbf{q}, E)|$  images. The line cuts were fitted to Gaussian peaks, and the locations of the peaks and the corresponding widths are shown as black circles with black lines. **d**,  $E$ - $q_x$  line cut through the sequence of measured  $|L(\mathbf{q}, E)|$  images. The line cuts were fitted to Gaussian peaks, and the locations of the peaks and the corresponding widths are shown as black squares with black lines. Note that the maximum intensity in **d** is 50% of the maximum intensity in **c** with respect to the colour bars.

$-15$  meV for the  $\alpha$ -band and  $+15$  meV to  $+25$  meV for the  $\epsilon$ -band in  $1.25$  meV steps), and then the mean of these amplitudes (black dots in Fig. 5c,d) was taken over the relevant energy range; the error bars represent the s.d. of the amplitude as the energy is varied. Figure 5c shows the measured  $L(\mathbf{q}, E)$  intensity of  $\alpha$ -band intraband QPI versus the  $q$ -space angles from Fig. 5a integrated over the energy range  $-25 \text{ meV} \leq E \leq -15 \text{ meV}$ , where this band is clear and distinct. Comparison with the theoretically predicted  $L(\mathbf{q}, E)$  intensity (blue dot-dash curve) versus  $\mathbf{k}$ -space angle for orbitally selective QPI with  $Z_{xy} \approx 0.1$ ,  $Z_{xz} \approx 0.2$  and  $Z_{yz} \approx 0.8$  (Supplementary Information Section VII) reveals good agreement. Similarly, comparison of the measured  $\epsilon$ -band  $L(\mathbf{q}, E)$  versus the  $q$ -space angles from Fig. 5b with the predicted  $L(\mathbf{q}, E)$  intensity (blue dot-dash curve in Fig. 5d) for orbitally selective quasiparticles having the same  $Z_{xy}:Z_{xz}:Z_{yz}$  ratios (Supplementary Information Section VII) yields  $Z_{xy} \sim 0$ . Therefore, the measured  $L(\mathbf{q}, E)$  amplitudes of QPI data (Fig. 5) are strongly consistent with orbital selectivity in the Hund's metal quasiparticles of FeSe for which  $Z_{xy} < Z_{xz} \ll Z_{yz}$ .

The measured  $Z_m$  phenomena in Figs. 2–5 reveal the strength of orbitally selective strong correlations in the normal metal state of FeSe. The data indicate that this metal has delocalized  $|\mathbf{k}\rangle$  states of  $d_{yz}$  character with good coherence because  $Z_{yz} \sim 1$ ,  $|\mathbf{k}\rangle$  states of  $d_{xz}$  char-

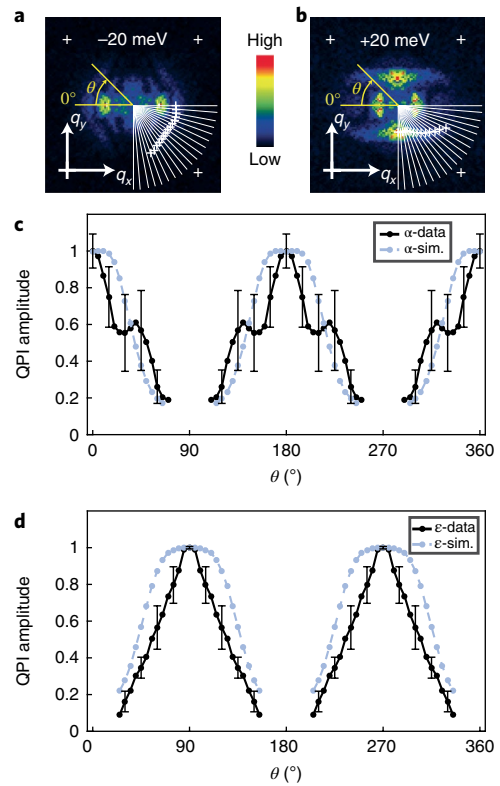


**Fig. 5 | Momentum-angle dependence of OSQP weight  $Z_m$ .** **a**, Measured  $|L(\mathbf{q}, E = -20 \text{ meV})|$  image from the  $\alpha$ -band showing the trajectory of the angularly resolved line cuts in **c**. Small white crosses mark the extracted peak location of QPI intensity; see Supplementary Information Section VII. The large white crosses correspond to  $\frac{3}{16} \left( \frac{2\pi}{a_{\text{Fe}}}, \frac{2\pi}{b_{\text{Fe}}} \right)$  points in momentum space.  $|L(\mathbf{q}, E)|$  is the amplitude of the Fourier transform of the normalized conductance ( $\equiv \left( \frac{dI}{dV} \right) / \left( \frac{I}{V} \right)$ ) at wavevector  $\mathbf{q}$  and energy  $E$ . **b**, Measured  $|L(\mathbf{q}, E = +20 \text{ meV})|$  image from the  $\epsilon$ -band showing the trajectory of angularly resolved line cuts in **d**. Small white crosses mark the extracted peak location of QPI intensity; see Supplementary Information Section VII. **c**, Measured mean  $L(\mathbf{q}, E)$  amplitude versus angle for the  $\alpha$ -band. The amplitudes are extracted from measured  $|L(\mathbf{q}, E)|$  images on the trajectory shown by crosses in **a**, and averaged over the  $-25$  to  $-15$  meV energy range, with the error bar showing the s.d. for the sequence of amplitudes at different energies. Blue symbols show the predicted values of  $|L(\mathbf{q}, E = -20 \text{ meV})|$  in the OSQP scenario with quasiparticle weights  $Z_{xy} \approx 0.1$ ,  $Z_{xz} \approx 0.2$  and  $Z_{yz} \approx 0.8$ . **d**, Measured mean  $L(\mathbf{q}, E)$  amplitude versus angle for the  $\epsilon$ -band. The amplitudes are extracted from measured  $|L(\mathbf{q}, E)|$  images on the trajectory shown by crosses in **b**, and averaged over the  $15$  to  $25$  meV energy range with the error bar showing the s.d. for the sequence of amplitudes at different energies. Blue symbols show the predicted values of  $|L(\mathbf{q}, E = +20 \text{ meV})|$  in the OSQP scenario with quasiparticle weights  $Z_{xy} \approx 0.1$ ,  $Z_{xz} \approx 0.2$  and  $Z_{yz} \approx 0.8$ .

acter that are significantly less coherent and  $|\mathbf{k}\rangle$  states of  $d_{xy}$  character with the lowest relative coherence. Comparison of the measured  $|L(\mathbf{q}, E)|$  with the theoretical  $|L(\mathbf{q}, E)|$  predictions for different ratios  $Z_{xy}:Z_{xz}:Z_{yz}$  (Fig. 2), along with evaluation of the  $\mathbf{k}$ -angle dependence of the QPI intensity for both bands (Fig. 5) (Supplementary Information Section VII), indicate that  $Z_{xy} < Z_{xz} \ll Z_{yz}$ . Moreover, we find the ratio of quasiparticle weights  $Z_{xy}:Z_{xz}:Z_{yz}$  producing good agreement between theoretical  $|L(\mathbf{q}, E)|$  and the QPI data  $|L(\mathbf{q}, E)|$  (Figs. 2, 3 and 4) to be indistinguishable from that deduced independently from the energy gap structure caused by orbital-selective Cooper pairing<sup>18,19</sup>. This provides strong support for the concept of

OSQP identification and Z quantification using QPI. Of most significance is that these orbital-selective QPI data provide a direct demonstration that the normal state from which the HTS emerges in FeSe is dominated by orbitally selective strong correlations. If true in general for the iron-based HTS materials this would be of fundamental significance, because strong electronic correlations would then play a central role in both copper-based and iron-based HTS.

**Data availability.** The data described in the paper are archived by the Davis Research Group at Cornell University and can be made available by contacting the corresponding author.

Received: 22 February 2018; Accepted: 24 July 2018;

Published online: 3 September 2018

## References

- Dagotto, E. Correlated electrons in high-temperature superconductors. *Rev. Mod. Phys.* **66**, 763 (1994).
- Georges, A., Kotliar, G., Krauth, W. & Rozenberg, M. J. Dynamical mean-field theory of strongly correlated fermion systems and the limit of infinite dimensions. *Rev. Mod. Phys.* **68**, 13 (1996).
- Paglione, J. & Greene, R. L. High-temperature superconductivity in iron-based materials. *Nat. Phys.* **6**, 645–658 (2010).
- Wang, F. & Lee, D. H. The electron-pairing mechanism of iron-based superconductors. *Science* **332**, 200–204 (2011).
- Haule, K. & Kotliar, G. Coherence–incoherence crossover in the normal state of iron oxypnictides and importance of Hund's rule coupling. *New J. Phys.* **11**, 025021 (2009).
- Yin, Z. P., Haule, K. & Kotliar, G. Kinetic frustration and the nature of the magnetic and paramagnetic states in iron pnictides and iron chalcogenides. *Nat. Mater.* **10**, 932–935 (2011).
- de' Medici, L., Mravlje, J. & Georges, A. Janus-faced influence of Hund's rule coupling in strongly correlated materials. *Phys. Rev. Lett.* **107**, 256401 (2011).
- Lanata, N. et al. Orbital selectivity in Hund's metals: the iron chalcogenides. *Phys. Rev. B* **87**, 045122 (2013).
- Georges, A., de' Medici, L. & Mravlje, J. Strong correlations from Hund's coupling. *Annu. Rev. Condens. Matter Phys.* **4**, 137–178 (2013).
- de' Medici, L., Giovannetti, G. & Capone, M. Selective Mott physics as a key to iron superconductors. *Phys. Rev. Lett.* **112**, 177001 (2014).
- Fanfarillo, L. & Bascones, E. Electronic correlations in Hund metals. *Phys. Rev. B* **92**, 075136 (2015).
- de' Medici, L. & Capone, M. In F. Mancini, R. Citro (eds) *The Iron Pnictide Superconductors*. Springer Series in Solid-State Sciences 186 (Springer, Cham, 2017).
- de' Medici, L. in *The Physics of Correlated Insulators, Metals, and Superconductors (Modeling and Simulation Vol. 7)* (eds Pavarini, E., Koch, E., Scalettar, R. & Martin, R.) 377–398 (Forschungszentrum Juelich, Juelich, 2017).
- de' Medici, L., Hassan, S. R., Capone, M. & Dai, X. Orbital-selective Mott transition out of band degeneracy lifting. *Phys. Rev. Lett.* **102**, 126401 (2009).
- Aichhorn, M., Biermann, S., Miyake, T., Georges, A. & Imada, M. Theoretical evidence for strong correlations and incoherent metallic state in FeSe. *Phys. Rev. B* **82**, 064504 (2010).
- Yu, R. & Si, Q. Mott transition in multiorbital models for iron pnictides. *Phys. Rev. B* **84**, 235115 (2011).
- Yu, R., Zhu, J.-X. & Si, Q. Orbital selectivity enhanced by nematic order in FeSe. Preprint at <https://arxiv.org/abs/1803.01733> (2018).
- Sprau, P. O. et al. Discovery of orbital-selective Cooper pairing in FeSe. *Science* **357**, 75–80 (2017).
- Kreisel, A. et al. Orbital selective pairing and gap structures of iron-based superconductors. *Phys. Rev. B* **95**, 174504 (2017).
- Arakawa, N. & Ogata, M. Orbital-selective superconductivity and the effect of lattice distortion in iron-based superconductors. *J. Phys. Soc. Jpn.* **80**, 074704 (2011).
- Yu, R., Zhu, J. X. & Si, Q. Orbital-selective superconductivity, gap anisotropy, and spin resonance excitations in a multiorbital  $t$ - $J_1$ - $J_2$  model for iron pnictides. *Phys. Rev. B* **89**, 024509 (2014).
- Yi, M., Zhang, Y., Shen, Z.-X. & Lu, D. Role of the orbital degree of freedom in iron-based superconductors. *npj Quantum Mater.* **2**, 57 (2017).
- Suzuki, Y. et al. Momentum-dependent sign inversion of orbital order in superconducting FeSe. *Phys. Rev. B* **92**, 205117 (2015).
- Watson, M. D. et al. Evidence for unidirectional nematic bond ordering in FeSe. *Phys. Rev. B* **94**, 201107 (2016).
- Watson, M. D., Haghighirad, A. A., Rhodes, L. C., Hoesch, M. & Kim, T. K. Electronic anisotropies revealed by detwinned ARPES measurements of FeSe. *New J. Phys.* **19**, 103021 (2017).
- Terashima, T. et al. Anomalous Fermi surface in FeSe seen by Shubnikov–de Haas oscillation measurements. *Phys. Rev. B* **90**, 144517 (2014).
- Watson, M. D. et al. Emergence of the nematic electronic state in FeSe. *Phys. Rev. B* **91**, 155106 (2015).
- Coldea, A. I. & Watson, M. D. The key ingredients of the electronic structure of FeSe. *Annu. Rev. Condens. Matter Phys.* **9**, 125–146 (2018).
- Capriotti, L., Scalapino, D. J. & Sedgewick, R. D. Wave-vector power spectrum of the local tunneling density of states: ripples in a d-wave sea. *Phys. Rev. B* **68**, 014508 (2003).
- Yuan, T., Figgins, J. & Morr, D. K. Hidden order transition in URu<sub>2</sub>Si<sub>2</sub>: evidence for the emergence of a coherent Anderson lattice from scanning tunneling spectroscopy. *Phys. Rev. B* **86**, 035129 (2012).
- Lee, J. et al. Heavy d-electron quasiparticle interference and real-space electronic structure of Sr<sub>2</sub>Ru<sub>2</sub>O<sub>7</sub>. *Nat. Phys.* **5**, 800–804 (2009).
- Schmidt, A. R. et al. Imaging the Fano lattice to 'hidden order' transition in URu<sub>2</sub>Si<sub>2</sub>. *Nature* **465**, 570–576 (2010).
- Allan, M. P. et al. Imaging Cooper pairing of heavy fermions in CeCoIn<sub>5</sub>. *Nat. Phys.* **9**, 468–473 (2013).
- Kasahara, S. et al. Field-induced superconducting phase of FeSe in the BCS–BEC cross-over. *Proc. Natl Acad. Sci. USA* **111**, 16309 (2014).
- Watahige, T. et al. Evidence for time-reversal symmetry breaking of the superconducting state near twin-boundary interfaces in FeSe revealed by scanning tunneling spectroscopy. *Phys. Rev. X* **5**, 031022 (2015).

## Acknowledgements

We are grateful to S.D. Edkins, A. Georges, M.H. Hamidian, J.E. Hoffman, G. Kotliar, E.-A. Kim, D.-H. Lee, L. de Medici, P. Phillips and J.-H. She for helpful discussions and communications. J.C.S.D. and P.C.C. acknowledge support from the Moore Foundation's EPIQS (Emergent Phenomena in Quantum Physics) Initiative through Grant No. GBMF4544 and Grant No. GBMF4411, respectively. P.J.H. acknowledges support from DOE Grant No. DE-FG02-05ER46236. A.Kr. and B.M.A. acknowledge support from a Lundbeckfond Fellowship (Grant No. A9318). Material synthesis and detailed characterization at Ames National Laboratory was supported by the U.S. Department of Energy, Office of Basic Energy Science, Division of Materials Sciences and Engineering—Ames Laboratory is operated for the U.S. Department of Energy by Iowa State University under Contract No. DE-AC02-07CH11358; experimental studies carried out by the Center for Emergent Superconductivity, an Energy Frontier Research Center, headquartered at Brookhaven National Laboratory, were funded by the U.S. Department of Energy under Contract No. DE-2009-BNL-PM015.

## Author contributions

A.Ko., Y.X.C. and P.O.S. developed and carried out the experiments; A.E.B. and P.C.C. synthesized and characterized the samples; A.Ko., P.O.S. and A.Kr. developed and carried out analysis; A.Kr., B.M.A. and P.J.H. provided theoretical guidance; B.M.A., P.J.H. and J.C.S.D. supervised the project and wrote the paper with key contributions from A.Ko., Y.X.C., P.O.S., A.Kr. and P.J.H. The manuscript reflects the contributions and ideas of all authors.

## Competing interests

The authors declare no competing interests.

## Additional information

**Supplementary information** is available for this paper at <https://doi.org/10.1038/s41563-018-0151-0>.

**Reprints and permissions information** is available at [www.nature.com/reprints](http://www.nature.com/reprints).

**Correspondence and requests for materials** should be addressed to J.C.S.D.

**Publisher's note:** Springer Nature remains neutral with regard to jurisdictional claims in published maps and institutional affiliations.